The Composite Response of Traveling Planetary Waves in the Middle Atmosphere Surrounding Sudden Stratospheric Warmings through an Overreflection Perspective

C. Todd Rhodes[1,2], Varavut Limpasuvan[1], Yvan Orsolini[3,4]

[1]Coastal Carolina University, Conway, South Carolina

[2]U.S. Naval Research Laboratory, Washington, District of Columbia

[3]NILU - Climate and Environmental Research Institute , Kjeller, Norway

[4]Norwegian University of Science and Technology, Trondheim, Norway

Corresponding Author: C. Todd Rhodes, ctrhodes@coastal.edu

Abstract

Traveling planetary waves surrounding sudden stratospheric warming events can result from direct propagation from below or *in situ* generation. They can have significant impacts on the circulation in the mesosphere and lower thermosphere. Our study runs a series of ensembles initialized from the Whole Atmosphere Community Climate Model, Version 4, nudged up to 50 km by six-hourly Modern-Era Retrospective Analysis for Research and Application, Version 2, reanalysis to compile a library of sudden stratospheric warming events. To our knowledge, we present the first composite or ensemble study that attempts to link direct propagation and *in situ* generation by evaluating the wave geometries associated with the overreflection perspective, a framework used to describe how planetary waves interact with critical and turning levels. The present study looks at the evolution of these interactions through the onset of sudden stratospheric warmings with an elevated stratopause or ES-SSWs. Robust and unique features of ES-SSWs are determined by employing an ensemble study that compares ES-SSWs with normal winters. Our study evaluates the production and impacts of westward-propagating, quasi-stationary, and eastward-propagating planetary waves surrounding ES-SSWs. Our results show that eastward-propagating planetary waves are generated within the westward stratospheric wind layer after ES-SSW onset which aids in restoring the eastward stratospheric wind. The interaction of quasi-stationary and westward-propagating waves with the westward stratospheric wind is explored from an overreflection perspective and reaffirms that westward-propagating planetary waves are produced from instabilities at the top of the westward stratospheric wind reversal.

1. Introduction

Occurring in ~50% of boreal winters, an enhancement of quasi-stationary planetary waves of zonal wavenumbers 1 and 2 can result in sudden stratospheric warmings or SSWs (e.g., Butler et al., 2015). Upon dissipation, these waves strongly decelerate the stratospheric flow, inducing an overturning mean meridional circulation that adiabatically warms the polar region. The anomalous polar warming causes the stratopause to descend below its climatological altitude (Matsuno, 1971). The coinciding wavenumber-1 and/or -2 pattern can project onto a dominant mode of climate variability in the troposphere called the Arctic Oscillation, a.k.a. the Northern Annular Mode (e.g., Baldwin & Dunkerton, 2001). Consequently, after a 10- to 30-day period following the stratospheric vortex disruption, the jet stream tends to shift equatorward over the Atlantic and anomalously cold conditions prevail over Europe and Northeast America.

As the perturbed polar vortex begins to recover from SSW, a new stratopause can reform at an altitude level at least 10 km above its norm (e.g., Manney et al., 2008; Siskind et al., 2010). These "elevated stratopause" SSW events (or ES-SSWs) reflect the strong coupling between the stratosphere and the mesosphere-lower thermosphere (MLT) region. This coupling is exemplified by an unusually strong polar downwelling during the stratopause reformation that transport long-lived tracers found in the thermosphere well into the stratosphere (e.g., Orsolini et al., 2022; Orsolini et al., 2017). During climatological wintertime conditions, downwelling over the pole is induced by westward GW drag near the stratopause. However, ES-SSW events give rise to the presence of strong traveling planetary (Rossby) waves around the time of ES-SSW onset (e.g., Iida et al., 2014; Limpasuvan et al., 2016). These waves can impose a significant impact on the circulation of the MLT (e.g., Rhodes et al., 2021; Sassi et al., 2016). Limpasuvan et al. (2016) found that strong WPWs in particular dissipate in the MLT and enhance downwelling over the pole. The presence of these waves further indicates the strong connection between the stratosphere and the overlying atmosphere.

Based on the composite of 13 ES-SSW events, Limpasuvan et al. (2016) reported a robust signature of eastward-propagating planetary waves (EPWs) that intensify approximately a week before ES-SSW onset (see their Figure 10). With roughly a 10-day period, these waves appear over the polar lower mesosphere region. Focusing on the 2009 ES-SSW event, past studies have shed new light on EPWs. Specifically, Iida et al. (2014) attributed the observed EPWs to local manifestations of barotropic/baroclinic instability in the lower mesosphere. EPW production relieved baroclinic instability and induced an eastward acceleration on the background flow, counteracting westward accelerations from dissipating quasi-stationary planetary waves or QSPWs (Iwao & Hirooka, 2021). Rhodes et al. (2021) suggested that these EPWs originate from the overreflection of upward-propagating EPWs from the lower stratosphere as they approach a region of strong wind shear (e.g., Harnik & Heifetz, 2007). The overreflection process then produces EPWs that emanate from the unstable region. Alternatively, Song et al. (2020) indicated that asymmetric gravity wave drag (GWD) in the lower mesosphere can locally generate EPWs that propagate downward into the lower stratosphere.

The new stratopause reformation following ES-SSW onset is accompanied by the slow westward-propagating planetary waves (WPWs). These WPWs are attributed mainly to barotropic/baroclinic instability of the westward polar stratospheric wind, fostered by the anomalous polar warming (Chandran et al., 2013b; Limpasuvan et al., 2012; Tomikawa et al., 2012). With periods between 5–12 days, the generated WPWs can propagate into the MLT. Their damping causes strong westward forcing above 80 km that can drive a strong polar downwelling and initiate the intense downward transport of long-lived tracers into the stratosphere (Orsolini et al., 2010). Forcing due to WPWs may help promote the MLT's recovery from ES-SSW and the conditions for the stratopause reformation at an elevated altitude (Limpasuvan et al., 2016).

The exact nature of EPWs and WPWs and their underlying mechanisms with respective to the ES-SSW phase (i.e., before or after onset) remain uncertain. This uncertainty stems from the small number of observed ES-SSW events that hinders our ability to develop a robust picture of these traveling waves. With the advent of satellite observations since 1980, fewer than 30 ES-SSWs had been identified. The aforementioned studies on these waves were largely based on case studies (particularly, the strong 2009 ES-SSW event) or composites of few events (Limpasuvan et al., 2016). As such, traveling waves are typically overlooked in the context of SSWs. However, having more knowledge of these waves and their roles during ES-SSWs may provide new insights into ES-SSWs, which are recognized as playing a major factor in the surface climate.

This study aims to better understand the sources and impacts of PWs of various phase speeds surrounding ES-SSW events. Our objectives are to (1) characterize the background flow, the associated wave structure, and their co-evolution, and (2) identify plausible sources that lead to the wave appearance. Our study leverages a unique ensemble numerical experimental setup that yields many ES-SSW events to develop a robust picture of EPWs and WPWs with respect to winters without ES-SSW. With this framework, we evaluate EPWs, QSPWs, and WPWs during three different time periods: before, 0 to 10 days after, and beyond 10 days after SSW onset. Our results indicate that EPWs generated by GW dissipation propagate within the region of westward stratospheric wind. EPW growth in this region applies an eastward acceleration, acting to restore the eastward stratospheric winds. Our study explores how QSPWs and WPWs interact with the westward stratospheric wind and reaffirms that WPWs are produced from instabilities at the top of the westward stratospheric wind reversal.

2. Background and Methods

The Whole Atmosphere Community Climate Model (WACCM), Version 4 developed at the National Center for Atmospheric Research (NCAR) is an atmosphere-only global chemistry-climate model extending up to ~145 km (Marsh et al., 2013). WACCM was run in the specified dynamics configuration (WACCM-SD) with a horizontal resolution of 0.95° latitude by 1.25° longitude, 88 vertical levels, and key dynamical variables output daily. In this configuration, the simulated temperature and dynamics were constrained up to 50 km with six-hourly Modern-Era Retrospective Analysis for Research and Application (MERRA) Version 2 reanalysis (Gelaro et al., 2017). Temperature and wind fields are nudged by 10% every 30 minutes through a mass-conserving interpolation of MERRA reanalysis onto the WACCM-SD horizontal grid. See Orbe et al. (2020) for tangential discussion on nudging experiments. A linear transition is applied between the nudged output below 50 km and the overlying, fully interactive, free-running region above 60 km. Run from 1980-2013, the WACCM-SD simulation constitutes the “base run” from which ensembles were generated.

2.1 SSW Identification and Classification in the Base Model Run

The definition of ES-SSW events varies significantly in previous studies such that the stratopause altitude has a discontinuity of 10 km (Limpasuvan et al., 2016), 15 km (Chandran et al., 2013a), and 18 km (Karami et al., 2023). With these criteria, ES-SSWs had frequencies of 5, 3, and 2 per decade, respectively. We identified ES-SSW events using the criteria from Limpasuvan et al. (2016). The criteria provide rigorous constraints on the upper stratosphere, which will be key in understanding the interaction of PWs in this region. Winters when none of these criteria are met persistently (i.e., lasting longer than 5 days) will be referred to as "normal winters". For example, a winter containing an SSW without an elevated stratopause would neither be classified as normal winter nor a winter containing an ES-SSW. For the remainder of the study, ES-SSWs will be identified simply as SSWs.

Four identified SSW events were selected from the base run (see **Table 1**) as reference cases for our ensemble experiments (described below). They have the SSW onsets dates of 12 February 1984, 9 January 2006, 22 January 2009, and 5 January 2013. These onset dates are in close agreement with observations, as expected since the model is nudged with observations. The first two SSW events are classified as "displaced type", characterized by the perturbed polar vortex shifting off the North Pole sufficiently to produce a SSW (Charlton & Polvani, 2007; Kuttippurath & Nikulin, 2012). The latter two events are "split type", where the separation of the polar vortex into two distinct vortices results in a SSW (Coy & Pawson, 2015; Kuttippurath & Nikulin, 2012; Manney et al., 2009).

2.2 Ensemble Setup

The four selected SSW events from the base run correspond to observations below 50 km (via nudging) and are free-running above 60 km. In setting up our ensemble experiment, we retain all the specified dynamics configurations noted above. However, we only nudge below the lower most model level with a linear transition to 0.4 km, leaving the higher levels as free-running. For a selected SSW event, we initialize each ensemble member by randomly perturbing the temperature field of the base run at 40 days prior to the event's reference SSW onset date shown in Table 1. The perturbation amount is below the model's rounding error of ~10^{-14} K (e.g., Kay et al., 2015). The 40-day lead time well exceeds the reported SSW predictability around 20 days (Domeisen et al., 2020; Karpechko, 2018) and allows for randomized outcomes.

Using the aforementioned identification criteria, this setup produced ensemble members with both SSW winters and normal winters (termed "SSW members" and "normal members", respectively). Some ensemble members are neither normal nor SSW members and were excluded from the results. For each selected SSW event, at least 10 normal members and 10 SSW members were generated. The amount of SSW and normal members collected for each event are shown in Table 1. In total, 76 SSW winters were and 68 normal winters were collected.

Reference SSW onset date (YYYY-MM-DD)	**Number of normal members**	**Number of SSW members**
1984-02-21	16	12
2006-01-09	12	33
2009-01-22	29	14
2013-01-05	11	17

Table 1. Number of normal and SSW ensemble members generated with respect to reference SSW onset dates.

2.3 Data Analyses

The meridional gradient of the zonal-mean quasi-geostrophic potential vorticity ($\bar{q}_\phi$) was used to examine the stability of the middle atmosphere (O'Neill & Youngblut, 1982):

$$\bar{q}_\phi = 2\Omega cos\phi - a^{-1}\left(\frac{(\bar{u}\cos\phi)_\phi}{\cos\phi}\right)_\phi - \frac{a\, f_0^2}{\rho_0}\left(\frac{\rho_0}{N_B^2}\bar{u}_z\right)_z \tag{1}$$

where ϕ is the latitude, z the log-pressure height, f_0 is the reference Coriolis parameter, ρ_0 is the reference density, Ω the Earth's angular frequency, and N_B is the Brunt-Väsälä frequency. The first term on the right-hand side (RHS) or the "beta term" is positive definite and associated with the gradient of f_0. The second term is the "barotropic term" associated with horizontal wind curvature. Lastly, the third term is the "baroclinic term" associated mainly with the vertical wind curvature. Computation of $\bar{q}_\phi$ was based on 3-day averages of the dependent field variables which inherently filtered out waves with periods < 3 days (c_x > 77 m·s^{-1} at 60°N). In the figures below, $\bar{q}_\phi$ is nondimensionalized by Ω.

Eastward, westward, and stationary components of diagnostics were optionally obtained by first implementing a 31-day sliding Hanning window to dependent field variables (wind, temperature, etc.) and applying a Fourier transform. The zonal phase speed of the wave, c_x, is related to $\bar{q}_\phi$ through the PW dispersion relation (Andrews et al., 1987).

$$c_x - \bar{u} = -\frac{\bar{q}_\phi}{k^2 + l^2 + \frac{f^2}{N_B^2}\left(m^2 + \frac{1}{4H^2}\right)} \tag{2}$$

where $H \approx 7km$ is the scale height. Generally, $\bar{q}_\phi$ is positive in the atmosphere and $c_x - \bar{u} < 0$ or the phase speed of the planetary wave is westward relative to the background wind. Beyond a level where $\bar{q}_\phi$ switches signs, $\bar{q}_\phi$ is negative and a PW can only exist if its phase speed is eastward relative to the zonal-mean zonal wind or $c_x - \bar{u} > 0$. Our study shows that the latter option is possible following the *in-situ* generation of EPWs. Additionally, as a PW approaches a critical layer, its wavelength approaches infinity and the PW becomes evanescent. This becomes evident if the denominator on the right-hand side is switched with the left-hand side of Equation 2.

The Eliassen-Palm (EP) flux and its divergence was computed using formulation associated with the transformed Eulerian-mean (TEM) equations given in Andrews et al. (1987). For these calculations, 5-day running averages were applied to dependent field variables (wind, temperature, etc.) to remove perturbations with periods < 5 days (or with c_x > 46 m·s^{-1} at 60°N).

The squared refractive index (n^2) can be used to better understand how PWs of certain zonal wavenumbers (s) and zonal phase velocites (c_x) propagate in $\bar{u}$ (Andrews et al., 1987):

$$n^2 = \frac{\bar{q}_\phi}{a\,(\bar{u} - c_x)} - \left(\frac{s}{a\,cos\phi}\right)^2 - \left(\frac{f_0}{2N_B H}\right)^2 \qquad (3)$$

PWs tend to propagate towards a large positive squared refractive index and are unable to propagate in regions with a negative squared refractive index. The boundary at which $n^2 = 0$ is called the turning level and the boundary at which $n^2 \rightarrow \pm\infty$ is the critical level.

However, the value of n^2 is difficult to composite as it varies widely, often approaching infinity. Instead, a critical level can be determined to occur when $\bar{u} - c_x = 0$. While the determination of the turning level involves all three terms in Equation 3, a comparison shows that the turning level can be approximated by $\bar{q}_\phi$ under specific conditions. While the third term remains relatively small ($\sim 10^{-13}$), the second and first terms can more comparable ($\sim 10^{-12}$). However, our study focuses on waves with low wavenumbers ($s \leq 6$) in regions near the PWs critical level ($\bar{u} - c_x$ near zero). Under these conditions, the first term will be dominant. Additionally, since the second and third terms will always be negative, a turning level must occur when $\bar{q}_\phi$ changes sign. Therefore, a sign change in $\bar{q}_\phi$ verifies that a turning level exists and approximates the position of the turning level in the context of our study.

2.4. Composites and Anomalies

Composites of the SSW members from all selected SSW events are made after aligning them with respect to their SSW onset date. The composite of the normal members was aligned with respect to the reference SSW onset date listed in Table 1. The alignment date is referred to as day 0. The risk of bias for a particular set of ensemble members (described by a row in Table 1) was eliminated by averaging the ensembles members in each set first, then averaging the sets together. Anomalies are calculated by subtracting the composited diagnostic across normal members from the composited diagnostic across SSW members. Assuming a Gaussian distribution of the diagnostic values at each location and time for SSW members and normal members (weighted such that each ensemble set has an equal contribution), the area where these distributions overlap was calculated. This area is the probability that a value found at a location and reference day during an SSW would also be found during a normal winter. Subtracting the area from unity gives the probability that, given an SSW occurrence, the diagnostic value will be different from that found during normal winters. Alternatively, it is the probability of being abnormal (Ab) given the occurrence of an SSW, which is henceforth abbreviated as P(Ab|SSW). Values of P(Ab|SSW) greater than 0.5 suggests that the anomaly is more likely than not associated with an SSW. These anomalies are good indicators of SSW occurrence. Although an anomaly may be large, a low P(Ab|SSW) suggests that the values is still large in scenarios when no SSW occurs. Thus, a large anomaly at this location and reference day may be associated with SSWs, but is not a good indicator for the occurrence of an SSW.

2.5 The Overreflection Perspective

An elegant perspective on the interaction of PWs with atmospheric boundaries comes from Lindzen et al. (1980) in which the zero isopleths of the relative PW phase velocity, $\bar{u} - c_x$, and of $\bar{q}_\phi$ serve as critical and turning levels, respectively. The diagnostic $\bar{q}_\phi$ is generally positive such that a region of negative $\bar{q}_\phi$ implies the presence of a zero-$\bar{q}_\phi$ isopleth. A critical level embedded inside a layer of negative $\bar{q}_\phi$ (and thus beyond a turning level) can act as a source of unstable PW growth (Dickinson, 1973). From an overreflection perspective, unstable PW growth is seeded by a PW tunneling past a turning level and amplifying at the critical level (e.g., Harnik & Heifetz, 2007). This perspective relates incident PWs (usually upward-propagating PWs from the troposphere) to the *in-situ* generation of PWs from instability. Depending on the relative positioning of the source level, turning level, and critical level, several wave geometries are possible. The wave geometries in **Figure 1** illustrate the interaction of PWs with the background wind shear where a PW critical level is expressed by the wind profile.

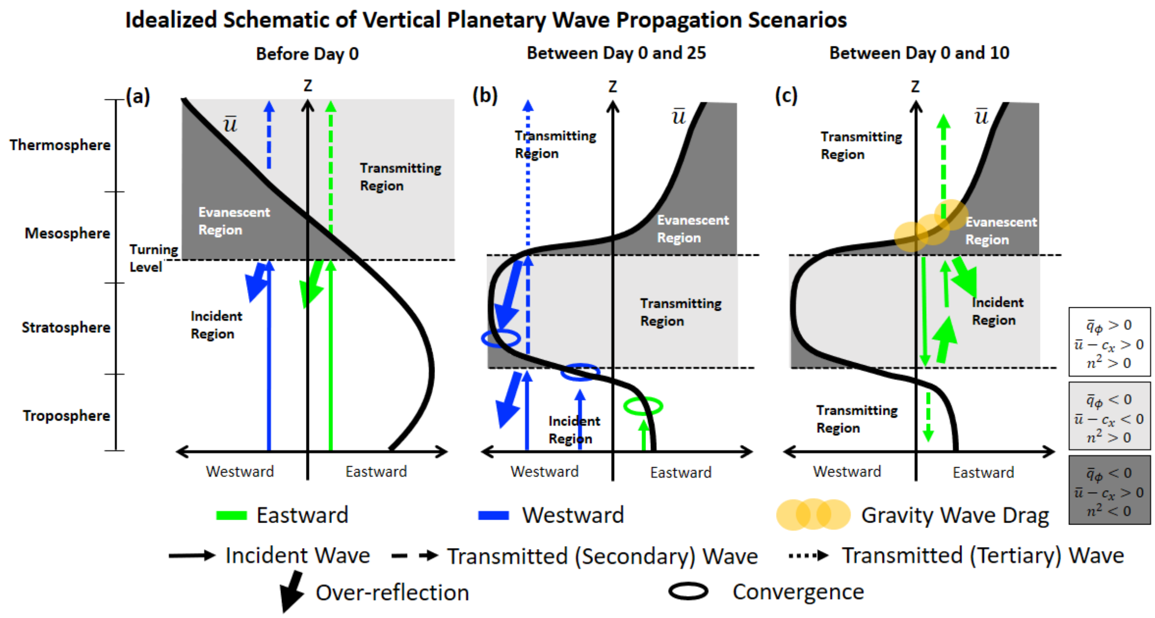

Figure 1. Wave geometries of vertical PW propagation between 20 km and 90 km through the evolution of the SSW. In our composite, these scenarios occur (a) before day 0, (b) day 0-25, and (c) day 0-10. The scenario in (c) is similar to (b) but focuses exclusively on PWs generated by asymmetric GWD. Angled arrows emphasize overreflection, but do not suggest any change in wave phase speed.

Figure 1a shows the wave geometry before SSW onset, which is similar to the winter climatology. Upward-propagating incident PWs (thin solid arrows) can overreflect if a perturbation is able to tunnel from the turning level (thin dashed line) to the critical level (thick solid line). This results in an overreflected wave below the turning level and a transmitted wave above the critical level. Overreflection and transmission are represented by thicker solid arrows and thin dashed arrows, respectively. The overreflected wave carries more energy than the incident wave; this wave energy growth can be indicated by EP flux divergence.

The evanescent region lies beyond the turning level where PW propagation is not possible. Here, a tunneling perturbation exponentially decays in amplitude. A thinner evanescent region would increase the likelihood of a PW being able to reach a boundary beyond the turning level. Additionally, the wave geometry a PW experiences depends on the zonal phase velocity of the wave. Blue and green arrows represent PWs with westward and eastward zonal phase velocities, respectively. Shown in Figure 1a, westward (eastward) waves would experience a thicker (thinner) evanescent region, making it more difficult (easier) to tunnel and stimulate PW growth at the critical level. Hence, phase velocity affects where a PW propagates and dissipates. While additional non-conservative considerations (such as asymmetric GW drag) are necessary, the overreflection perspective connects incident, transmitted, and overreflected waves to one another.

Notably, our study uses composites with respect to an SSW onset date. During individual SSW cases, overreflection could occur at different relative times or not occur at all. Our study seeks to evaluate general trends in PW growth and dissipation during an SSW event.

2.6 Asymmetric Gravity Wave Drag

A multiwave parameterization is implemented in WACCM such that a momentum flux vs. phase speed function is represented by a set of discretized GWs. Separate parameterizations are implemented for GWs sourced from orography, convection, and frontogenesis. At the source level, the GW is launched and momentum flux is distributed directly aloft depending on the background winds. Detailed discussion on WACCM's GW parameterization can be found in Appendix A of Garcia et al. (2007) and in Richter et al. (2010). Even for parameterized GWs in WACCM, the background winds will influence where and how much momentum flux is deposited.

The troposphere may not be the only source mechanism for PWs in the middle atmosphere. The preferential filtering of GWs by the underlying stratospheric winds can result in zonally asymmetric GW drag in the MLT (Smith, 2003). Lieberman et al. (2013) showed that the wintertime characteristics of MLT perturbations were qualitatively consistent with a simple model of dissipating GWs generating a wavenumber-1 PW after being filtered by underlying stratospheric PW perturbations. Ultimately, the GW-induced ageostrophic winds would result in a divergence (convergence) pattern mirroring the stratospheric high-pressure (low-pressure) regions below (Lieberman et al., 2013). Resultantly, PW perturbations would be imprinted on the MLT by flow divergence induced by GWs that survived the wind perturbations in the stratosphere.

3. Results

The stratosphere maintains an eastward flow throughout a normal winter and experiences an eastward-to-westward wind reversal during winters with SSWs. The zonal-mean zonal wind during normal winters and winters with SSWs are shown in **Figure 2**. For normal winters (Figure 2a), the mesospheric zero-wind line is maintained at 82.6 km with a standard deviation of 12.4 km based on the altitude of the mesospheric zero-wind line. This was calculated with zonal wind values collected 41 days surrounding the reference SSW onset date (Table1) of each normal ensemble member. During winters with SSWs (Figure 2b), the zero-wind line rapidly descends leading to wind reversal at 1hPa on day 0. The stratopause (thick black dotted line) is maintained around 60 km during normal winters (Figure 2a). While the altitude of the stratopause and the timing of its post-onset reformation are not consistent between ensemble members, the stratopause discontinuity and altitude change can still be depicted in the composite. During winters with SSWs (Figure 2b), the stratopause descends rapidly upon SSW onset to ~50 km. Roughly around 15-25 days after onset, the stratopause reforms at ~60km which results in a >10 km vertical discontinuity.

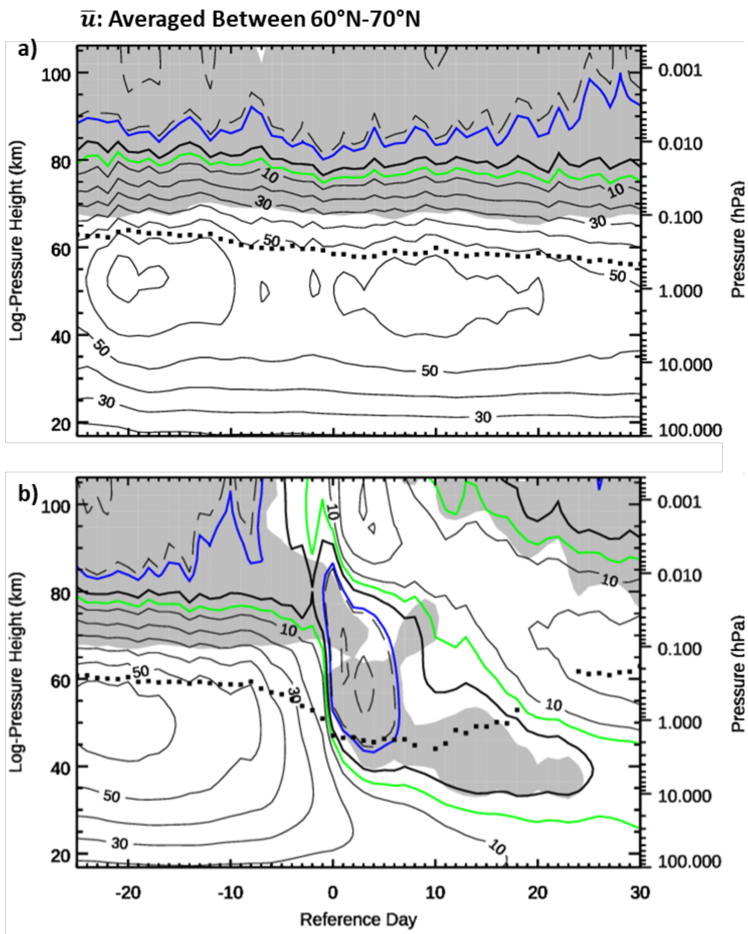

Figure 2. Height-time composites of $\bar{u}$ averaged from 60-70°N during (a) normal and (b) SSW winters. $\bar{u}$ is shown by thin black contours and is incremented by 10 m s^{-1}. Blue and green lines emphasize the location of the -8 and 5 m s^{-1} isotachs, respectively. Grey shading shows regions of negative $\bar{q}_{\phi}$. The thick dotted line indicates the location of the stratopause where the temperature maximum exceeds 237K; locations where this criterion is not met more than 25% of the time are excluded.

Ultimately, the stark contrast between a steady zero-wind line during normal winters and a dramatically descending zero-wind line during SSW winters depends on the stability of the mesospheric flow. The stability of the flow is diagnosed by $\bar{q}_{\phi}$, such that sign changes in $\bar{q}_{\phi}$ (edges of the shaded regions in Figure 2) indicate a turning level.

Being a part of a composite study, the exact position of critical levels for EPWs, QSPWs, and WPWs vary between ensemble members and cannot be explicitly shown. However, **Figure 3** shows the composited phase speed distribution of geopotential height perturbation amplitude, $\widetilde{Z_g}$, for planetary waves at 0.001 hPa, 0.01 hPa, 0.1 hPa, and 10 hPa. At 10 hPa, a large $\widetilde{Z_g}$ is present for QSPWs (near-zero c_x) throughout SSW evolution. This is expected since quasi-stationary PWs are primarily responsible for the demise of the polar vortex. At 0. 1 hPa and above (Figures 3a-c), the phase speed distribution of $\widetilde{Z_g}$ becomes more spread out. To distinguish the characteristics of traveling and quasi-stationary waves, WPWs, QSPWs, and EPWs are defined to have zonal phase velocities ranging $(-\infty,\ -8)$, $(-8, 5)$, and $(5, \infty)$ m s^{-1}, respectively. The -8 and 5 m s^{-1} phase speeds that separate these regimes are shown as dashed horizontal lines. Notably, since c_x distribution of $\widetilde{Z_g}$ extends farther westward than eastward after SSW, the c_x boundary between WPWs and QSPWs is set farther from the zero-c_x line. In doing so, the characteristics of WPWs can be better visualized without as much influence from the quasi-stationary component.

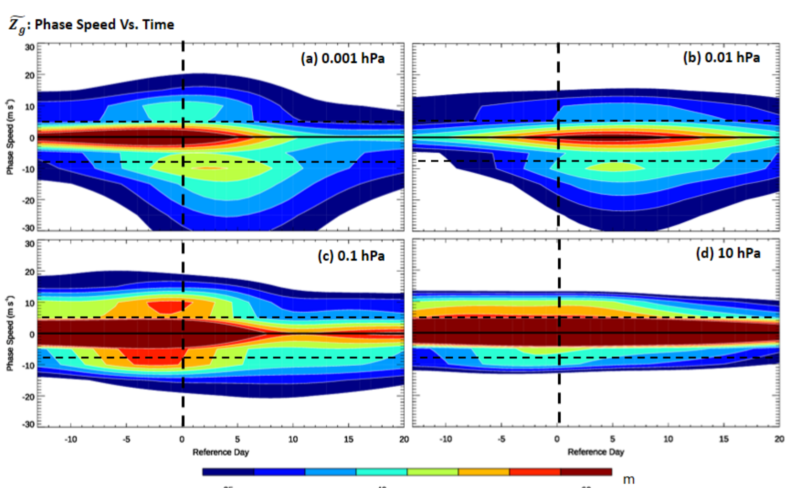

Figure 3. Phase speed vs. time composites of $\widetilde{Z_g}$ in meters at (a) 0.001 hPa (b) 0.01 hPa, (c) 0.1 hPa, and (d) 10 hPa.

In Figure 2, blue (green) contours emphasize the -8 (5) m s^{-1} isotachs that separate the wind regimes containing critical levels for WPWs, QSPWs, and EPWs. EPWs would find their critical level outside green contours (winds greater than 5 m s^{-1}), QSPWs between green and blue contours, and WPWs beyond blue contours (winds less than -8 m s^{-1}). However, the ability for PWs to reach their critical level depends on the stability of the zonal-mean flow.

In **Figure 4a**, positive (red-shaded contours) and negative (grey-shaded contours) $\bar{q}_\phi$ values are an indicator of the stability of the background flow. The grey-shaded regions show where the necessary, but not sufficient, condition for instability is fulfilled. In **Figure 4b**, the dominance of beta, barotropic, and baroclinic terms of $\bar{q}_\phi$ (see Equation 1) are shown by blue, grey, and red shading, respectively. A term is determined to be dominant if it has the largest magnitude relative to the other compositional terms. A negative (positive) contribution of the dominant term is indicated by a darker (lighter) shading. For example, since the planetary vorticity is always positive in the Northern Hemisphere, the beta term is always shown by light blue shading. The zero-wind line (thick black contour) separates the regions of mean eastward and westward flow.

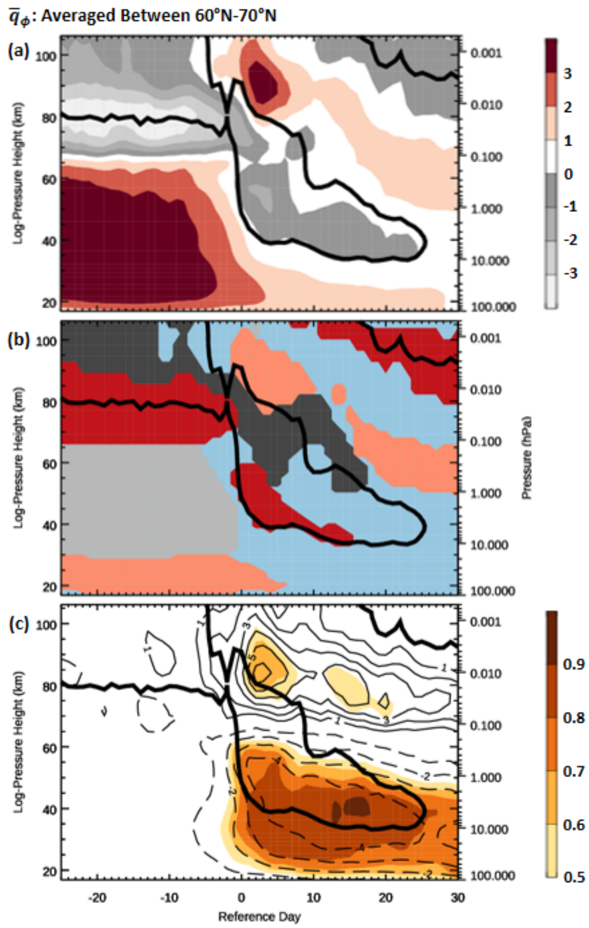

Figure 4. Height-time (a,b) composites and (c) anomalies of $\overline{q}_\phi$ during SSW winters. (a) Positive (negative) $\overline{q}_\phi$ values are shown by red (grey) shaded contours. $\overline{q}_\phi$ is dimensionless after dividing by Earth's angular velocity. (b) Dominance of the beta, barotropic, and baroclinic terms are indicated by blue, grey and red regions, respectively. Lighter/darker shades of a color indicate a positive/negative contribution of the dominant term. (c) Positive (negative) anomalies of $\overline{q}_\phi$ are indicated by solid (dashed) contours. The probability that the anomaly is abnormal is given by orange-shaded contours. The zero-wind line is indicated by a thick solid contour.

Prior to SSW events, the background flow in the middle atmosphere only becomes baroclinically unstable (indicated by a dark red-shaded region in Figure 4b) due to the curvature of wind shear as the wind transitions from eastward in the mesosphere to westward in the lower thermosphere. This baroclinic instability could be exacerbated by the westward wind bias in the lower thermosphere of WACCM, hypothesized to be due to the omission of secondary or higher order GWs. However, during times of a more perturbed vortex like a SSW period, model winds are closer to observations (Harvey et al., 2022).

Figure 4c shows positive (negative) $\bar{q}_{\phi}$ anomalies in solid (dashed) contours with orange-shaded contours indicating P(Ab|SSW), as explained in Section 2.4. Small $\bar{q}_{\phi}$ anomalies and low P(Ab|SSW) values before day -10 indicate that negative $\bar{q}_{\phi}$ in the MLT is common during normal winters too, also shown in Figure 2a. In Figure 2a, critical levels for WPWs, QSPWs, and EPWs exist past the turning level during a normal wintertime MLT, shown by the -8 m s^{-1}, 5m s^{-1}, and zero-wind isotachs embedded in the $\bar{q}_{\phi} < 0$ (shaded) region. Similar to the schematic in Figure 1a, eastward-propagating waves (EPWs) would experience a thinner evanescent region, having a critical level closer to the turning level than QSPWs or WPWs. Therefore, overreflection would be more favorable towards EPW production during a normal winter. If a PW cannot tunnel through the evanescent region, the wave is refracted meridionally, and variability in the mesospheric zero-wind line is curtailed. A similar wave geometry is seen before day 0 in Figure 2b. Rhodes et al. (2021) discusses how the zonal wind configuration leading up to SSW onset becomes conducive for the overreflection of EPWs.

The zonal-mean zonal wind is closely tied to $\bar{q}_{\phi}$ in the middle atmosphere with a correlation coefficient of 0.98. This coefficient was calculated from the averaged values of the zonal-mean zonal wind and $\bar{q}_{\phi}$ between 10 hPa and 1 hPa, 60°N and 70°N, and day -20 and 30 across all SSW ensemble members. Given this high correlation, $\bar{q}_{\phi}$ can be used as a proxy diagnostic for the zonal-mean zonal wind in the middle atmosphere. For example, around day 5, the westward wind becomes weaker in Figure 1b and corresponds to diminishing magnitudes of negative $\bar{q}_\phi$ in Figure 4a. Therefore, the stabilization of the stratospheric winds can be gauged by increased $\bar{q}_\phi$, in which positive $\bar{q}_\phi$ and eastward zonal-mean winds are restored upon SSW recovery. Approaching onset in Figure 4a-b, the normally unstable baroclinic flow in the mesosphere starts to stabilize, indicated by the increase in $\bar{q}_\phi$, mostly from the barotropic term.

Figure 4 reveals three distinct wind configurations are present surrounding an SSW, which can be evaluated across three notable periods. Sections 3.1, 3.2, and 3.3 address periods of no reversed stratospheric wind layer (before day 0), a thick reversed stratospheric wind layer (day 0 – 10), and a thin reversed stratospheric wind layer (after day 10), respectfully. Subordinate sections are differentiated by PW phase speed such that the origins and impacts of WPWs, QSPWs, and EPWs are assessed for each scenario.

3.1 No Reversed Stratospheric Wind Layer – Before Day 0

3.1.1 WPW and QSPW Interaction with No Reversed Stratospheric Wind Layer – Before Day 0

EP flux indicates the amount of energy transported by a PW and its convergence (divergence) depicts the deposition (absorption) of energy by the PW in the form of heat and momentum. For the quasi-geostrophic case, the meridional and vertical components of EP flux are related to momentum and heat, respectively (Andrews et al., 1987). Therefore, EP flux shows the direction of wave propagation and flux convergence (divergence) indicates wave deposition (growth). **Figure 5a-c** depicts the composited EP fluxes for (a) WPWs, (b) QSPWs, and (c) EPWs such that the color-filled contours indicate vertical flux while the blue (red) contours show EP flux convergence (divergence). Brown-filled contours in Figure 5a-c indicate that QSPWs have an exponentially greater upward flux than WPWs or EPWs prior to SSW. This is expected since QSPWs are the main driver of SSWs. **Figures 5d-f** shows positive (negative) EP flux divergence anomalies in solid (dashed) contours. Orange-shaded contours show P(Ab|SSW). Five or more days prior to SSW onset, this probability is low, suggesting that EP flux convergence/divergence is not a good indicator of SSW occurrence. From day -5 to day -1, QSPW flux convergence anomalies and P(Ab|SSW) become larger as QSPWs induce SSW onset.

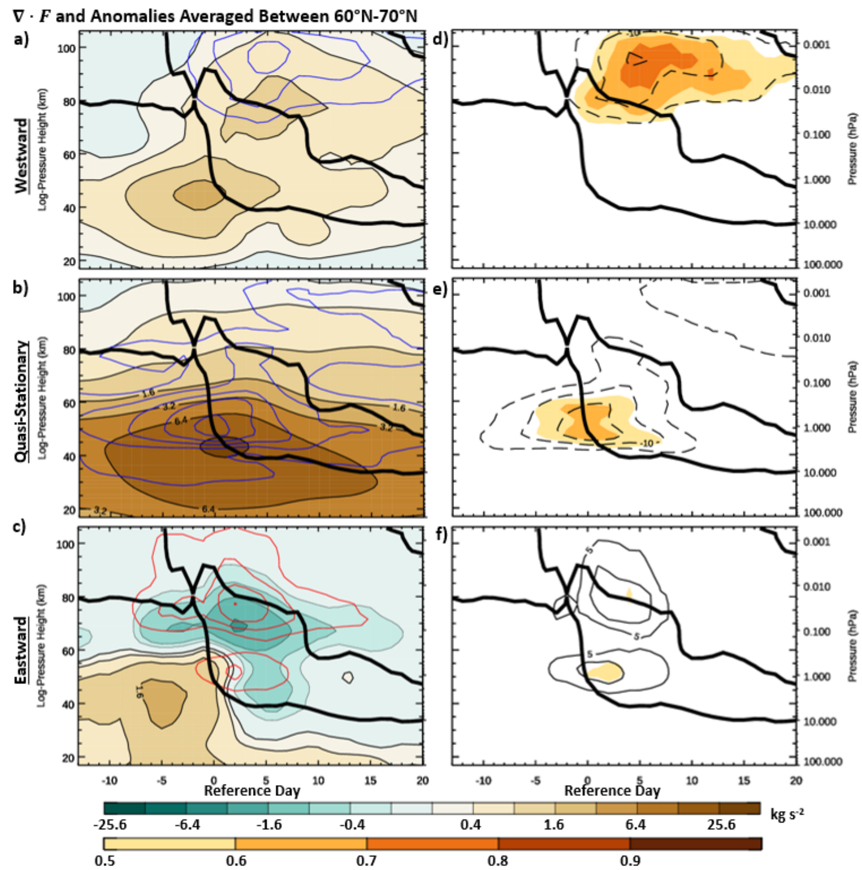

Figure 5. Height-time plots averaged between 60°N and 70°N comparing fluxes of (a,d) WPWs, (b,e) QSPWs, and (c,f) EPWs. (a-c) Upward (downward) vertical EP fluxes shown in tan (blue) shadings and are outlined by black regular-sized (thin) contours incremented by +(-) 0.2×2^i $\mathrm{kg\ s^{-2}}$ where i can be $[1,2,3,4,5,6,7,8]$. EP flux convergence (blue contours) and divergence (red contours) are incremented by $2\ \mathrm{m\ s^{-1}\ day^{-1}}$. (d-f) Positive (negative) anomalies of EP flux divergence are indicated by solid (dashed) contours and increment by 5 $\mathrm{m\ s^{-1}\ day^{-1}}$. The probability that the anomaly is abnormal is given by orange-shaded contours. The zero-wind line is indicated by a thick bold contour.

Figure 6 shows EP flux for WPWs, QSPWs, and EPWs organized by row, on different reference days, organized by column. Similar to Figure 5, red (blue) contours represent EP flux convergence (divergence) and the zero-wind line is represented by a thick black contour. Depending on the column, relevant isotachs that approximate the critical level are also included.

Similar to winters devoid of SSWs in Figure 2a, Figure 2b shows that prior to day 0 a thick layer of negative $\bar{q}_{\phi}$ encompasses the critical levels of WPWs and QSPWs. According to the first term in Equation 3, $\bar{q}_{\phi}$ is proportional to n^2 such that n^2 is negative when $\bar{q}_{\phi}$ is zero. As a result, PW group velocities are refracted away from the turning level and become less vertically oriented. This is exemplified in Figures 6a,d,g as high-latitude EP flux vectors turn southward with height**.**

Resultantly, PWs around 65°N are inhibited from propagating to their critical level aloft, which exist beyond the turning level. However, the -8, 0, and 5 m s^{-1} isotachs (blue, thick black, and green contours) show that EPWs experience the thinnest evanescent region. Therefore, it has the best chance of tunneling to its critical layer.

3.1.2 EPW Interaction with No Reversed Stratospheric Wind Layer – Before Day 0

As during a normal winter, discussed in the Section 3 introduction, the wave geometry at 70 km before SSW onset favors the overreflection of EPWs. This is evidenced by comparing Figures 5a-c; divergence near the stratopause prior to SSW is evident only in the eastward component of the flux. Figure 6g shows the EPW flux from a height-latitude perspective. EP flux divergence (red contour) occurs near a critical layer (bold green line) within a $\bar{q}_{\phi} < 0$ region (grey shading). EPW flux vectors emanate from this region and propagate equatorward and downward. Shown by blue-shaded contours in Figure 5c, this downward flux persists at 75 km from days -8 to 18 and extends into the stratosphere from days 3 to 9. The flux divergence feature in Figure 6g is associated with incident upward-propagating EPWs from below further suggesting overreflection.

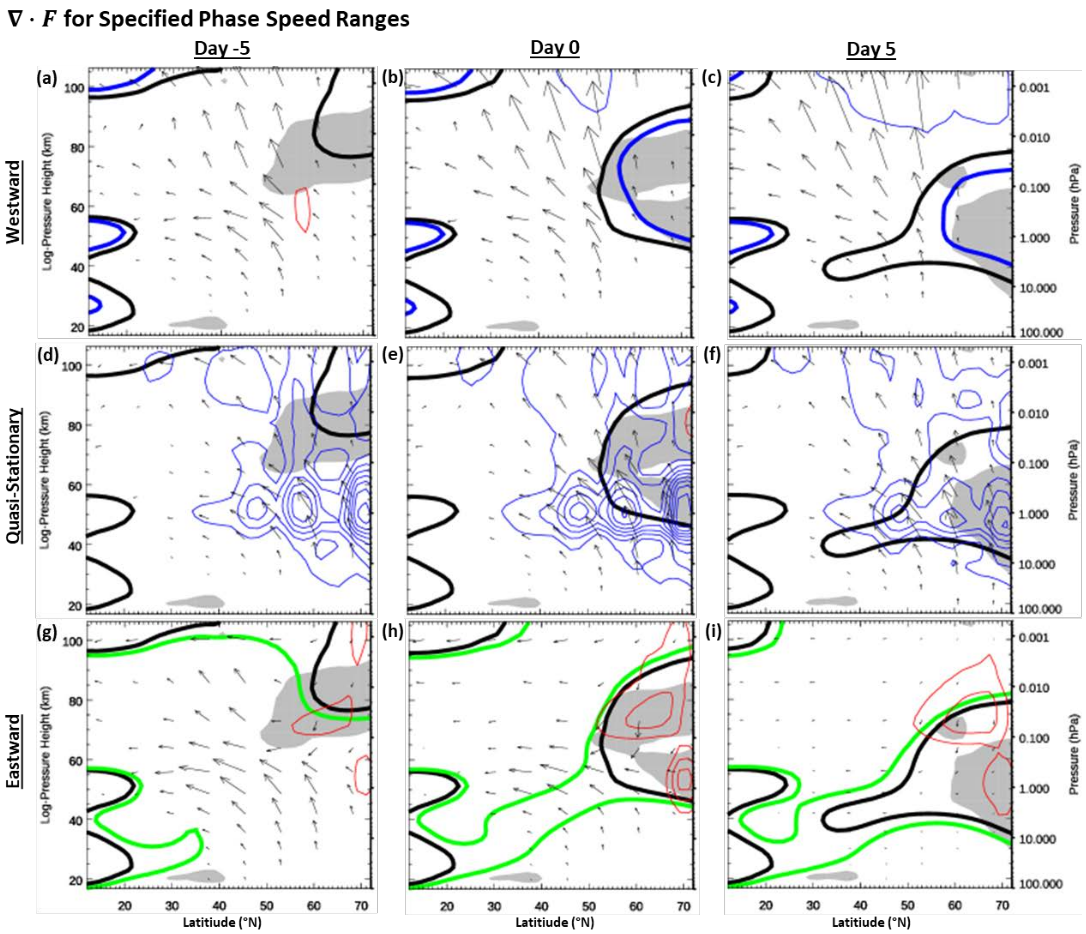

Figure 6. Height-latitude plots of (a-c) WPW, (d-f) QSPW, and (g-i) EPW EP flux divergence/convergence on (a,d,g) day -5, (b,e,h) day 0, and (c,f,i) day 5 shown in red/blue contours and incremented by 5 m s^{-1} day^{-1}. The meridional EP Flux vector component was scaled by $(100\pi a\rho)^{-1}\cos\phi$ and the vertical component by $(a\rho)^{-1}\cos\phi$. Regions of $\bar{q}_{\phi} < 0$ are shaded grey. The zero-wind line is indicated by a thick bold contour. As in Figure 2, thick blue (green) lines approximate WPW (EPW) critical layers at the -8(5) m s^{-1} isotachs.

Approaching onset, Figure 5c shows that a persistent upward flux doesn't only sustain a region of EP flux divergence but coincides with an increasing amount of EP flux divergence at 70 km approaching SSW onset. This is consistent with the overreflection mechanism; as the evanescent region becomes thinner (as shown in Figure 4a), incident waves more easily overreflect. In Figure 5c, the EPW EP flux divergence increases in tandem with $\bar{q}_\phi$ (shown in Figure 4a). Overreflection acts to relieve instability, but in doing so it reduces negative $\bar{q}_\phi$ that separates upward-propagating PWs from the critical level. A positive feedback loop is established in which upward-propagating PWs become increasingly effective at stabilizing the stratopause the longer they persist.

Figure 5f at 70 km shows small average EP flux divergence anomalies with P(Ab|SSW) < 0.1. While EP flux divergence for EPWs is a robust feature prior to SSW growth, the flux divergence at a specific height and reference day (with respect to SSW onset) is not a good indicator for SSW occurrence. Additionally, the low P(Ab|SSW) for all PWs prior to onset (in Figures 5d-f) suggests that the strength of the tropospheric forcing may not be the only factor in producing an SSW. The persistence of upward PW propagating (and increasing wave overreflection) may be just as important in initiating an SSW event.

3.2 Thick Reversed Stratospheric Wind Layer – Day 0 to Day 10

3.2.1 WPW Interaction with a Thick Reversed Stratospheric Wind Layer - Day 0 to Day 10

Days 0-10 are marked by descended westward winds in the stratosphere and eastward winds in the MLT, resulting in a layer of reversed stratospheric winds that has a zonal-mean westward flow persisting for over 2 weeks. WPWs with more westward phase velocities than the zonal wind speed would propagate past the reversed stratospheric winds unencumbered, while WPWs with slower phase velocities would experience a critical level and interact with the reversed stratospheric winds (compare blue arrows in Figure 1b). Since $\widetilde{Z_g}$ for WPWs with faster westward phase velocities than -20 m s^{-1} is small compared to slower WPWs (see Figure 3), we focus on the interaction of WPWs with the reversed stratospheric winds to explain their propagation through the middle atmosphere.

In Figure 2b, WPWs with phase velocities between -8 m s^{-1} (blue line) and -20 m s^{-1} would experience their critical level past a turning level and could overreflect. At the upper boundary of the reversed stratospheric winds, the turning level generally remains within the reversed stratospheric winds. Around day 4, the -10 m s^{-1} isotach rests above a turning level at the upper boundary of the reversed stratospheric winds. Therefore, WPWs slower than roughly -10 m s^{-1} would be prone to overreflect at both the bottom and top boundaries, each time extracting energy from the background flow and producing an overreflected and transmitted PW at each boundary (as suggested in Figure 1b). The transmitted components would compound and result an amplified WPW aloft. As a composite, these wave geometries are approximated by the average $\bar{q}_{\phi}$ and $\bar{u}$. In individual case studies, a wider range of phase velocities may be able to overreflect at both boundaries.

Compared to EPWs and QSPWs, WPWs have a relatively strong upward EP Flux (brown shading) above 80 km (cf., Figures 5a-c). An EP flux convergence region exceeding 20 m s^{-1} day $^{-1}$ in Figure 5a (blue contours) at ~95 km shows that WPW dissipation has a significant impact on the background wind. This abnormal EP flux convergence is unique to SSWs with P(Ab|SSW) > 0.6 (shown in Figure 5d). The enhanced upward EP flux and EP flux convergence for WPWs at high latitudes above 80 km are also evident in Figure 6c.

Figure 7 shows $\widetilde{Z_g}$ for WPWs, QSPWs, and EPWs. While WPW $\widetilde{Z_g}$ decreases around 55 km after SSW onset in Figure 7a, WPWs still maintain a presence within the reversed stratospheric winds. This is indicative of the limited phase velocity range of WPWs allowed to be transmitted into the reversed stratospheric winds. Since WPWs exist in the stratosphere during the normal winter, their $\widetilde{Z_g}$ values within the reversed stratospheric winds are not shown to be an abnormal anomaly associated with SSWs (Figure 7d). However, enhanced WPW $\widetilde{Z_g}$ in the MLT are unique to SSWs with P(Ab|SSW) > 0.6. The association of WPWs and SSWs agrees with studies by Kinoshita et al., (2010), Tomikawa et al., (2012), and Limpasuvan et al. (2016).

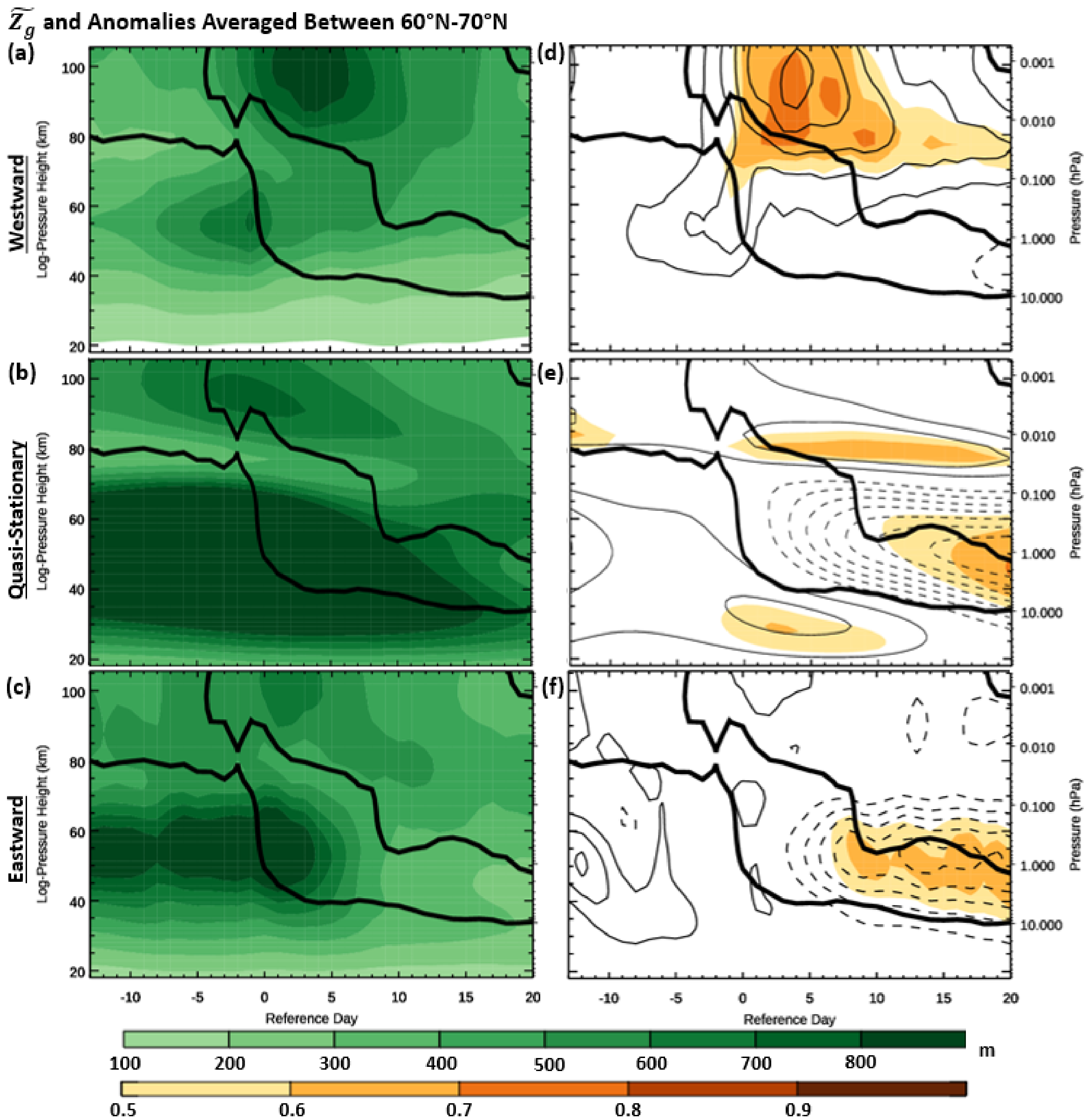

Figure 7. Height-time plot averaged between 60°N and 70°N. (a-c) Geopotential height perturbation amplitudes, $\widetilde{Z_g}$, are incremented by 100 m (d-f) Positive (negative) $\widetilde{Z_g}$ anomalies are indicated by solid (dashed) black contours incremented by 100 m. The probability that the anomaly is abnormal is given by orange-shaded contours. In all sub-plots, the zero-wind line is indicated by a thick bold contour.

3.2.2 QSPW Interaction with a Thick Reversed Stratospheric Wind Layer - Day 0 to Day 10

The zero-wind line is the critical level for stationary PWs which contain much of the upward flux relative to traveling PWs (cf., Figures 5a-c). On day -5 (Figure 6d), the zero-wind line is embedded in a region of negative $\bar{q}_\phi$ (grey shading). With their critical level beyond a turning level, upward-propagating PWs are refracted away from the zero-wind line. The intrusion of the zero-wind line into a region of positive $\bar{q}_\phi$ at day 0 (Figure 6e) greatly enhances n^2 through the first term in Equation 3. As a result, PW group velocities are directed toward the mesospheric zero-wind line, becoming more vertically oriented. Their subsequent convergence at the zero-wind line causes the isotach to drastically descend by more than 40 km. QSPWs have the largest flux convergence in this region by a magnitude of 10. Between the 40-65km region of Figure 5e, there is a significantly large flux convergence anomaly associated with the descent of the zero-wind line with P(Ab|SSW) > 0.5.

As expected, Figure 7b shows a QSPW $\widetilde{Z_g}$ upon SSW onset exceeding 800 m. Interestingly, low values of P(Ab|SSW) and $\widetilde{Z_g}$ in Figure 7e suggests that these QSPWs amplitudes are not abnormal. Therefore, a good indicator for SSW occurrence is not the large QSPW amplitude alone but rather the large QSPW EP Flux convergence anomaly.

3.2.3 EPW Interaction with a Thick Reversed Stratospheric Wind Layer - Day 0 to Day 10

Interestingly, flux divergence for EPWs at 75 km continues to increase after SSW onset (Figure 5c). This continued flux divergence is surprising from the overreflection perspective since an upward-propagating EPW should encounter a critical level before the turning level. Illustrated in Figure 1b, the presence of EPWs (green arrow) in the reversed stratospheric winds should not be possible by upward-propagating EPWs since they would experience a critical level and dissipate in the lower stratosphere. Both Figure 2b and Figure 6i show the positioning of the green contour at the bottom of the reversed stratospheric winds well outside of the grey-shaded region. Nevertheless, Figure 5c indicates that flux divergence occurs at both 50 and 70 km from day 0-5. These two layers of flux divergence forming at the top and bottom of the reversed stratospheric winds are a common feature, appearing in most of our ensembles at varying NH latitudes and heights. In Figure 5f, a flux divergence anomaly exceeding 10 m s^{-1} day^{-1} with a low P(Ab|SSW) suggests that, while the feature is present, it does not consistently occur at a specific space or time relative to SSW onset. Figure 7c shows that elevated values of EPW $\widetilde{Z_g}$ in the stratosphere persist several days after onset. As a common feature after SSW onset, the happenstance of nonlinear interaction is an insufficient explanation. During SSW, the polar vortex is shifted off the pole, resulting in zonally asymmetric mesospheric GWD (discussed in Section 2.6). The polar vortex shifts over different longitudes depending on the SSW. To help remove zonal phase variability during vortex breakdown, values are composited with respect to the average phase of the stratospheric wavenumber-1 Z_g' between 10 and 5 hPa such that the Z_g' ridge is always centered at 0° longitude.

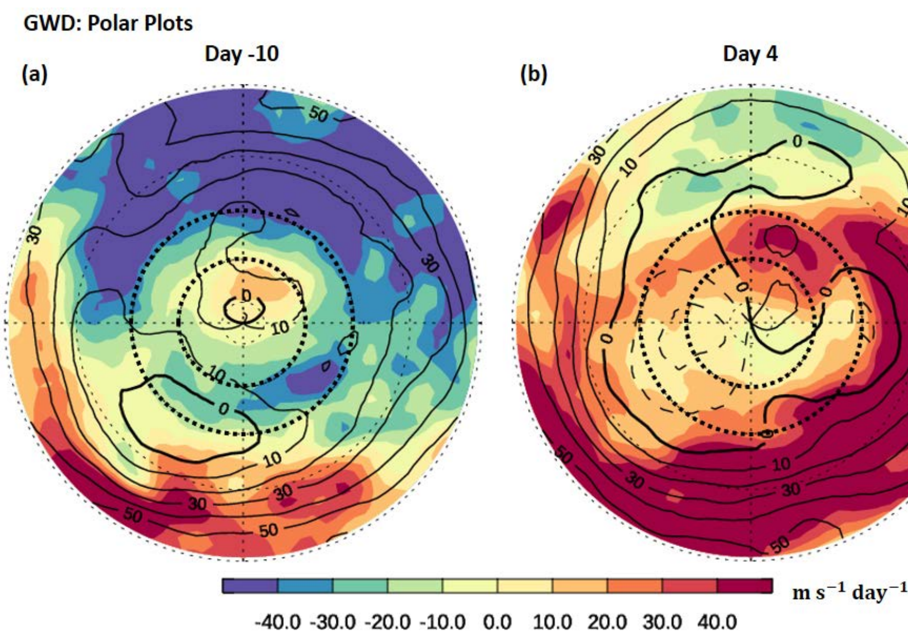

Figure 8. Polar plots of zonal GWD and zonal wind averaged from 0.1-0.01 hPa (a) 10 days before and (b) 4 days after SSW onset. Before compositing, the average phase from 10-5 hPa of the wavenumber-1 Z_g' is aligned such that the ridge is

centered at 0° longitude. Zonal lines (dotted) increment by 90°. Meridional lines (dotted) increment by 10° with 60°N and 70°N in bold. GWD is shown by colored shading in 10 m s^{-1} day^{-1} increment. Eastward (westward) zonal wind is overlaid in solid (dashed) contours which increment by 10 m s^{-1}. The zero-wind line is in bold.

Figure 8 shows the composited GWD at days -10 and 4 averaged between 0.1 and 0.01 hPa. GWD is then smoothed by 15° longitude and 10° latitude running mean. While westward GWD dominates on day -10 due to filtering from eastward winds below, eastward GWD at 0° longitude indicates that some eastward-propagating GWs are able to propagate through the stratospheric wavenumber-1 Z_g' ridge. On day 4, after the vortex displaces off the pole and zonal-mean stratospheric wind becomes westward, eastward GWD dominates. However, westward GWD at 180° longitude indicates that westward-propagating GWs are able to make it through the eastward winds of the stratospheric PW trough. The GWD has a large wavenumber-1 component, which can be isolated for a simplified visualization.

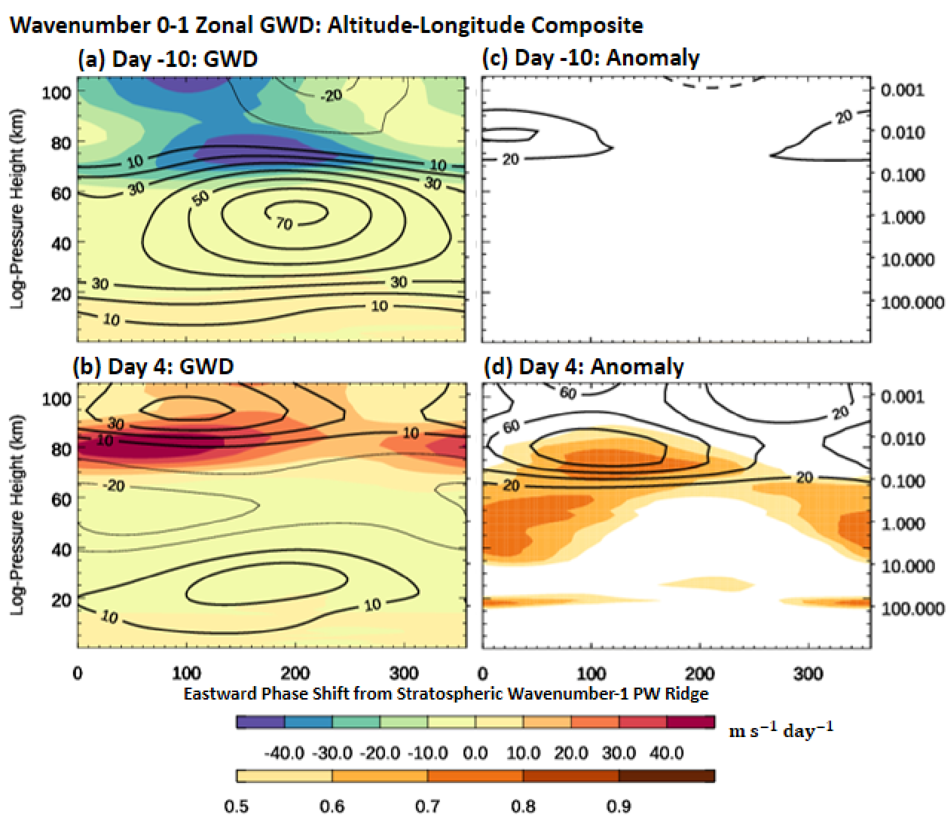

Figure 9. Altitude vs. relative phase shift of zonal GWD averaged between 60°N and 70°N. Before compositing, the average phase from 10-5 hPa of the wavenumber-1 Z_g' is aligned such that the ridge is centered at 0° longitude. (a,b) GWD is in filled contours and overlaid by the westward (eastward) wind velocity in thin (bold) contours. (c,d) Orange-shaded contours show P(Ab|SSW) and are overlaid by positive (negative) GWD anomalies in solid (dashed) black contours.

This asymmetric GWD averaged from 60-70°N (bold latitude lines in Figure 8) is further examined in **Figure 9** with respect to $\bar{u}$ (line contours). Figure 9 only looks at features of wavenumbers 0 and 1 to focus on the zonal-mean diagnostic and the relative effect of wavenumber-1 geopotential height perturbations, Z_g'. While patterns of wavenumbers greater than 1 may be relevant for specific cases, wavenumber-1 perturbations are common surrounding SSWs resulting from both split and displaced polar vortices (Bancalá et al., 2012).

On day -10 near 75 km (Figure 9a), westward GWD caps the strong eastward winds. Expectedly, this GWD is not significantly different than during normal winters, illustrated by low probability values in Figure 9c. Four days after SSW between 40 and 80 km, the stratospheric low-pressure system with strong eastward wind (thick black contours in Figure 9a) is replaced by a stratospheric high-pressure system with strong westward winds (thin black contours in Figure 9b) that constitute the reversed stratospheric winds region. The westward wind favors the transmission of eastward-propagating GWs, which impose an eastward GWD above the reversed stratospheric winds. This eastward GWD has a large wavenumber-1 component with the greatest GWD occurring between a 0° and 100° phase shift from the stratospheric wavenumber-1 PW ridge. Figure 9d shows an anomaly exceeding 60 m s^{-1} day^{-1} near 75 km with a P(Ab|SSW) > 0.7. As noted by Siskind et al. (2010) and Limpasuvan et al. (2012), the capping of the reversed stratospheric winds by eastward GWD is a reliable consequence of SSWs.

Hovmöller diagrams of GWD are overlaid with geopotential height, Z_g, (**Figure 10a**) and zonal wind (**Figure 10b**) contours averaged from 0.1-0.01 hPa and 60-70°N. Their comparison shows the interaction of GWD with regions of low and high pressure (indicated by regions of low and high Z_g, respectively). As in Figure 9, diagnostics show wavenumber-0 and -1 features and are composited with respect to the stratospheric wavenumber-1 geopotential. From approximately day 0 to 10, a region of increasingly high Z_g shifts and replaces a region of low Z_g. This coincides with the formation of the reversed stratospheric winds layer associated with the movement of a high-pressure system over the pole (seen as the development of stratospheric negative $\bar{q}_\phi$ in Figure 4a). As discussed for Figure 9, filled contours in Figure 10a,b show that GWD switches from a westward to an eastward forcing with a large wavenumber-1 component.

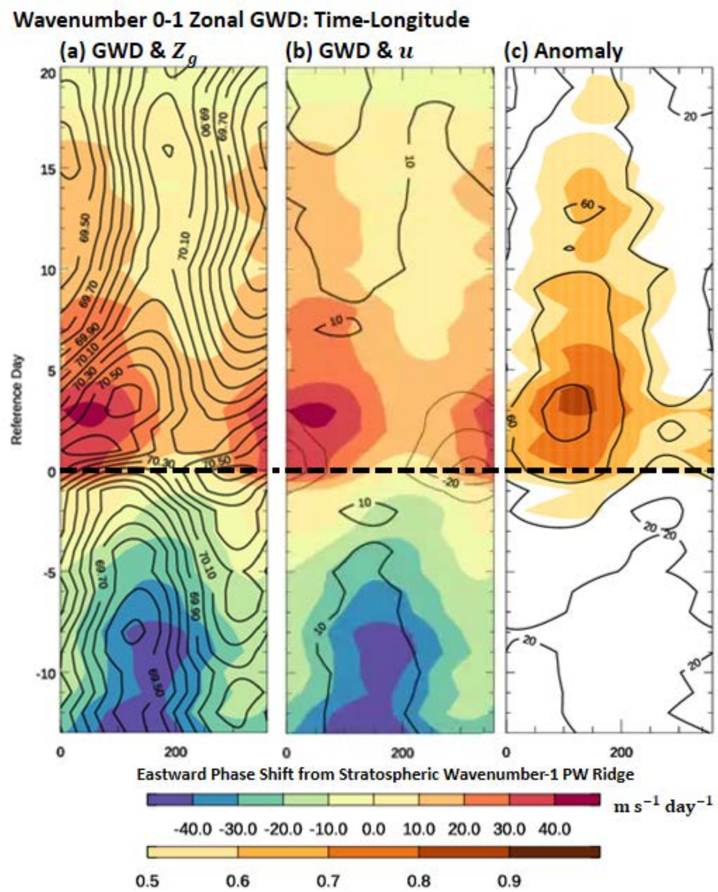

Figure 10. Time vs. relative phase shift of zonal GWD averaged from 60-70°N and 0.1-0.01 hPa. Before compositing, the average phase from 10-5 hPa of the wavenumber-1 Z_g' is aligned such that the ridge is centered at 0°. This longitudinal

shift is applied to all variables including GWD and zonal wind. (a) GWD is displayed by filled contours and overlaid by (a) geopotential height and (b) zonal wind in black contours. (c) Orange-shaded contours show P(Ab|SSW) and are overlaid by positive (negative) GWD anomalies in solid (dashed) black contours. The bold dashed line indicates SSW onset.

GWs propagate through the stratospheric wavenumber-1 Z_g ridge, shown by the phase shift, and dissipate on the westward (eastward) side of the mesospheric wavenumber-1 Z_g ridge (trough) shown in reference to Z_g contours. GWD counteracts the underlying westward winds (shown in Figure 9b and Figure 10b). This GWD is significant with an anomaly exceeding 80 m s^{-1} day^{-1} and P(Ab|SSW) > 0.8 (**Figure 10c**). The forcing manifests a wavenumber-1 EPW, shown in Figure 10a by an eastward shift in the high-pressure system over time between day 0 and day 10.

In order for asymmetric GWD to directly generate an EPW, an eastward migration of the asymmetry would be expected. However, this does not occur. Therefore, the phase speed of the generated EPW must be a result of the wave geometry where GWD occurs. In other words, asymmetric GWD seeds a region of unstable flow. The wave geometry that the PWs are born into allow them to extract energy from the flow and grow, taking on a phase speed equal to the background wind. Resultantly, EPW growth can be seen in Figure 5c near 80 km. After day 10, eastward GWD subsides as a low-pressure system indicated by low values of geopotential height reforms in this region (Figure 10a).

Interestingly, this interaction manifests as an EPW that has a destructive interference with the high-pressure system resulting in an overall loss of $\widetilde{Z_g}$ at 80 km. The growth of this wave acts to restore a low-pressure system to the stratosphere. This restoration is particularly evident in Figure 4a as $\bar{q}_\phi$ becomes positive at this level. An abnormally large positive $\bar{q}_\phi$ (red-shaded contours) due to an enhanced vertical wind curvature (indicated by light red shading in Figure 4b) appears around day 10 and 85 km with P(Ab|SSW) > 0.6. The decrease in wave activity in this region due to GWD could produce a dynamically quiet region and support an enhancement of $\bar{q}_\phi$ due to relaxation of the atmosphere towards thermal wind balance. The radiative relaxation rate near the stratopause is roughly 5-7 days (Gille & Lyjak, 1986) which agrees with the time scale of the $\bar{q}_\phi$ enhancement.

In Figure 10, eastward GWD forcing is seen around 50° longitude a few days before onset. In Figure 5c, EPW growth also begins a few days before onset. Therefore, the EPWs generated from instability prior to SSWs and may be one contiguous feature ultimately enhancing the stability of the mesosphere.

In Figure 5c, EPW flux divergence likewise occurs at the bottom of the reversed stratospheric winds which suggests another region of EPW wave growth. The wind structure and $\bar{q}_\phi$ between days 0 and 5 in Figure 2b is similar to the schematic in Figure 1c. For this wind configuration, upward-propagating EPWs would be absorbed by an exposed critical level. However, Figure 4c suggests that wave growth occurs around 45 km. This region of flux divergence can be explained when wave growth from asymmetric GWD is incorporated into the overreflection perspective. Figure 1c illustrates that if EPW are generated at the upper level of the reversed stratospheric winds and if the upper and lower levels of the reversed stratospheric winds are conducive to overreflection, they could become trapped. The trapping of these EPWs is supported by Figure 7c as $\widetilde{Z_g}$ for EPWs remains enhanced inside the reversed stratospheric winds after onset. The eastward accelerations at the bottom and top of the reversed stratospheric winds would modulate the thickness and duration of the reversed stratospheric winds, albeit convergence from upward-propagating PWs would also play a role.

3.3 Thin Reversed Stratospheric Wind Layer - After Day 10

3.3.1 WPW and QSPW Interaction with a Thin Reversed Stratospheric Wind Layer - After Day 10

Although weaker than between days 0-10, values of WPW $\widetilde{Z_g}$ (Figure 7a) and EP flux convergence (Figure 5a) are present above the reversed stratospheric winds. WPW flux convergence in the mesosphere was found to contribute to SSW recovery by promoting the reformation and descent of the stratopause around 80 km (Limpasuvan et al., 2016). The reformation of the stratopause begins around day 10 as westward mesospheric winds reform in a region of negative $\bar{q}_\phi$ as in the pre-SSW period (grey shading in Figure 4a), decreasing the baroclinic stability (dark red contours in Figure 4b).

Before day 10, QSPWs were absorbed by the reversed stratospheric winds. After day 10 (see Figure 7b), a region of enhanced $\widetilde{Z_g}$ persists on the lower boundary of the reversed stratospheric winds. Since P(Ab|SSW) < 0.5 at the lower boundary of the reversed stratospheric winds (Figure 7e), the $\widetilde{Z_g}$ magnitude is not abnormal, given that large QSPW $\widetilde{Z_g}$ often exists in the normal winter stratosphere. However, a negative $\widetilde{Z_g}$ anomaly at 50 km with P(Ab|SSW) > 0.5 indicates that there is an abnormal decrease in QSPW $\widetilde{Z_g}$ near the upper reversed stratospheric winds boundary. Therefore, while QSPWs exist at the bottom reversed stratospheric winds boundary, they are being absorbed in this region before they can propagate to the upper reversed stratospheric winds boundary.

After day 10, the flux convergence of QSPWs in the MLT increases around 90 km (Figure 5b). As the composited winds weaken and reverse, the likelihood of QSPWs propagating past the reversed stratospheric winds and impacting the MLT increases. Figure 5e shows the QSPW flux convergence anomaly in the MLT. The associated low P(Ab|SSW) likely results from large variations in the positioning of the stratopause or in tropospheric forcing after day 10. In Figure 7e, positive $\widetilde{Z_g}$ anomaly with P(Ab|SSW) > 0.6 confirms that the presence of QSPWs in the mesosphere are associated with SSW recovery. A lower turning level results in a thicker evanescent region for WPWs making it harder for them to overreflect. Additionally, the zonal-mean westward winds become weaker than -5 m s^{-1}. Faster WPWs with phase velocities less than -5 m/s wind will propagate past the reversed stratospheric winds unencumbered, but not extract any energy from the background flow from overreflection. Resultantly, WPW flux convergence in the MLT decreases while QSPW flux convergence increases after day 10.

3.3.2 EPW Interaction with a Thin Reversed Stratospheric Wind Layer - After Day 10

In the scenario shown in Figure 1b, EPWs are unable to propagate past the reversed stratospheric winds and are trapped in the troposphere. In Figure 7f, a negative $\widetilde{Z_g}$ anomaly near 50 km with P(Ab|SSW) > 0.6 shows that the stratosphere is devoid of EPWs during SSW.

Discussed in Section 3.2.3, eastward acceleration near the upper boundary of the reversed stratospheric winds is aided by the overreflection of EPWs seeded by GWs. After day 10, EP flux divergence associated with eastward GWD diminishes as the upper boundary of the reversed stratospheric winds descends below 60 km. The larger density below 60 km would reduce the amount of drag produced from GW momentum deposition and therefore reduce the effectiveness of GWD as a source for EPW growth. Without EPW overreflection providing additional aid to vortex recovery, the reversed stratospheric winds may remain in the lower stratosphere for prolonged periods of time.

The descended region of negative $\bar{q}_{\phi}$ remains closer to the lower boundary than the upper boundary of the reversed stratospheric winds: in Figure 4c, a significant negative anomaly in $\bar{q}_{\phi}$ with P(Ab|SSW) > 0.8 has its maxima located on the bottom reversed stratospheric winds boundary around 35 km. These features suggest that the prolonged reversed stratospheric winds in the stratosphere is being maintained by EPW and QSPW dissipation at the bottom of the reversed stratospheric winds, while dynamics at top of the reversed stratospheric winds act to restore the eastward flow. This is supported by schematics in Figure 1c where the bottom boundary of the reversed stratospheric winds absorbs QSPWs and EPWs due to an exposed critical level. On the other hand, the top boundary of the reversed stratospheric winds can relieve instability through the overreflection of EPWs inside the reversed stratospheric winds region, eastward GWD, or a relaxation to thermal wind conditions due to a lack of wave activity.

4. Conclusion

The overreflection perspective was applied to explain PW behaviors with various wave geometries. During normal winters, an unstable mesosphere inhibits QSPW absorption near the zero-wind line by establishing a turning level below. Approaching SSW, a positive feedback loop is created by persistent PW interaction with a thinning evanescent region that vertically orients stratospheric PWs and increases the likelihood of overreflection. This overreflection tends to produce waves with eastward phase velocities, illustrated by a persistent EP flux divergence around 70 km in Figure 5c. The resulting EPW growth acts to prevent the descent of the mesospheric westward wind into the stratosphere, counteracting effects of upward-propagating QSPWs (Iwao & Hirooka, 2021; Rhodes et al., 2021). After sufficient thinning of the evanescent region, the critical level becomes exposed to upward-propagating PWs and results in a rapid decent of the zero-wind line.

After day 0, GWD acts as a source mechanism on the upper boundary of the reversed stratospheric winds. EPWs can become trapped resulting in two layers of EP flux divergence at the top and bottom boundaries of the reversed stratospheric winds. To our knowledge, this is the first time this feature has ever been discussed. Additionally, WPWs can tunnel into the reversed stratospheric winds region, overreflect, and dissipate in the MLT. The production of WPWs from instability was also described by Kinoshita et al. (2010), Tomikawa et al. (2012), and Limpasuvan et al. (2016). The reversed stratospheric winds are maintained in the stratosphere due to tropospheric QSPW forcing suggested by the close proximity of the turning level and zero-wind line in the lower portion of the reversed stratospheric winds. The persistence of tropospheric forcing is just as important as the strength of tropospheric forcing in inducing SSWs, as found in re-analyses and forecast models (Orsolini et al., 2018).

The present study shows that SSW recovery has an evolving wave geometry that can support downward and upward vertical EP flux, properties of both reflective and absorptive SSWs, respectively, noted in Kodera et al. (2016). Additionally, the quicker recovery of reflective SSWs with downward vertical EP flux shown by Kodera et al. (2016) is indicative of overreflection; a period of strong overreflection would act to restore the polar vortex by inducing an eastward acceleration.

Additionally, a significant presence of WPWs in the MLT after SSW onset agrees with Limpasuvan et al. (2016), which identifies instability as their source mechanism. Sassi et al. (2016) also identifies WPWs in the MLT and shows that they can significantly impact the mean meridional circulation, enhancing upwelling in the tropics and downwelling at the pole. Enhanced polar downwelling can result in a descent of more nitric oxides produced from energetic particle precipitation at high latitudes, and case studies have shown that WPWs play a key role in modulating this descent in the MLT (Harvey et al., 2021; Orsolini et al., 2017). Harvey et al. (2021) found in a case study of the January 2009 SSW that the longitudinal asymmetry of the polar vortex impacts meridional circulation such that descent rates are 5 times larger within a PW trough. While further research is needed, our study offers a mechanism by which the reversed stratospheric winds can modulate PW phase velocities present in the MLT during SSW recovery.

The overreflection perspective implements critical layer theory to create a framework in which to evaluate PW interaction with various boundaries in the middle atmosphere. The present study shows that PW wave geometries are sensitive to their phase speeds, resulting in drastically different interactions with regions of varying winds like the reversed stratospheric winds. While our composite study shows the general influences of PWs relative to SSW onset, case studies may offer further insight on wave dynamics affecting SSW development that are not particularly correlated to the onset date.

Acknowledgements

CTR is supported by funding from the National Science Foundation (NSF) awards (RUI 1642232; REU 1560210). VL is supported by NSF Intergovernmental Panel Agreement. Edits were completed while C.T.R. held a National Research Council Research Associateship award at the U.S. Naval Research Laboratory. The authors acknowledge the computing and technical support from the NCAR Computation Information Systems Laboratory as well as the Coastal Carolina University cyberinfrastructure (CCU CI) project, funded in part by NSF award MRI 1624068. The authors also recognize the assistance of Dr. Stephen Eckermann in this study’s publication.

Data Availability Statement

The relevant daily model output can be accessed through the CCU CI at https://mirror.coastal.edu/sce/CTR_SSWEnsembles.

References

Andrews, D. G., J. R. Holton, and C. B. Leovy, 1987: *Middle Atmosphere Dynamics*. Academic Press.

Baldwin, M. P., and T. J. Dunkerton, 2001: Stratospheric harbingers of anomalous weather regimes. *Science (1979)*, **294**, 581–584, https://doi.org/10.1126/science.1063315.

Bancalá, S., K. Krüger, and M. Giorgetta, 2012: The preconditioning of major sudden stratospheric warmings. *Journal of Geophysical Research Atmospheres*, **117**, 1–12, https://doi.org/10.1029/2011JD016769.

Butler, A. H., D. J. Seidel, S. C. Hardiman, N. Butchart, T. Birner, and A. Match, 2015: Defining sudden stratospheric warmings. *Bull Am Meteorol Soc*, 1913–1928, https://doi.org/10.1175/BAMS-D-13-00173.1.

Chandran, A., Collins, R. L., Garcia, R. R., Marsh, D. R., Harvey, V. L., Yue, J., & De La Torre, L., 2013a: A climatology of elevated stratopause events in the whole atmosphere community climate model. *Journal of Geophysical Research Atmospheres*, **118**, 1234–1246. https://doi.org/10.1002/jgrd.50123.

Chandran, A., Garcia, R. R., Collins, R. L., & Chang, L. C., 2013b: Secondary planetary waves in the middle and upper atmosphere following the stratospheric sudden warming event of January 2012. *Geophysical Research Letters*, **40**, 1861–1867. https://doi.org/10.1002/grl.50373.

Charlton, A. J., and L. M. Polvani, 2007: A New Look at Stratospheric Sudden Warmings. Part I: Climatology and Modeling Benchmarks. *J. Climate*, **20**, 470–488, https://doi.org/10.1175/JCLI3994.1.

Coy, L., and S. Pawson, 2015: The major stratospheric sudden warming of January 2013: Analyses and forecasts in the GEOS-5 data assimilation system. *Mon Weather Rev*, **143**, 491–510, https://doi.org/10.1175/MWR-D-14-00023.1.

Dickinson, R. E., 1973: Baroclinic Instability of an Unbounded Zonal Shear Flow in a Compressible Atmosphere. *J. Atmos. Sci.*, **30**, 1520–1527.

Domeisen, D. I. V., and Coauthors, 2020: The Role of the Stratosphere in Subseasonal to Seasonal Prediction: 1. Predictability of the Stratosphere. *Journal of Geophysical Research: Atmospheres*, **125**, 1–17, https://doi.org/10.1029/2019JD030920.

Garcia, R. R., D. R. Marsh, D. E. Kinnison, B. A. Boville, and F. Sassi, 2007: Simulation of secular trends in the middle atmosphere, 1950–2003. *J. Geophys. Res*., **112**, D09301, doi:10.1029/2006JD007485.

Gelaro, R., and Coauthors, 2017: The modern-era retrospective analysis for research and applications, version 2 (MERRA-2). *J Clim*, **30**, 5419–5454, https://doi.org/10.1175/JCLI-D-16-0758.1.

Gille, J. C., and L. v. Lyjak, 1986: Radiative heating and cooling rates in the middle atmosphere. *Journal of Atmospheric Sciences*, **43**, 2215–2229.

Harnik, N., and E. Heifetz, 2007: Relating Overreflection and Wave Geometry to the Counterpropagating Rossby Wave Perspective: Toward a Deeper Mechanistic Understanding of Shear Instability. *J Atmos Sci*, **64**, 2238–2261, https://doi.org/10.1175/JAS3944.1.

Harvey, V. L., S. Datta-Barua, N. Pedatella, C. E. Randall, D. E. Siskind, and W. E. van Caspel, 2021: Transport of nitric oxide via Lagrangian Coherent Structures into the top of the polar vortex. *J. Geophys. Res.: Atmos*, **126**, e2020JD034523. https://doi.org/10.1029/2020JD034523.

——, Pedatella, N., Becker, E., & Randall, C. 2022: Evaluation of polar winter mesopause wind in WACCMX+DART. *Journal of Geophysical Research: Atmospheres*, **127**, e2022JD037063. https://doi.org/10.1029/2022JD037063.

Iida, C., Hirooka, T., & Eguchi, N., 2014: Circulation changes in the stratosphere and mesosphere during the stratospheric sudden warming event in January 2009. *Journal of Geophysical Research: Atmospheres*, **119**, 7104–7115. https://doi.org/10.1002/2013JD021252.

Iwao, K., and T. Hirooka, 2021: Opposite Contributions of Stationary and Traveling Planetary Waves in the Northern Hemisphere Winter Middle Atmosphere. *Journal of Geophysical Research: Atmospheres*, **126**, https://doi.org/10.1029/2020JD034195.

Karami, K., Borchert, S., Eichinger, R., Jacobi, C., Kuchar, A., Mehrdad, S., Pisoft, P., & Sacha, P., 2023: The Climatology of Elevated Stratopause Events in the UA-ICON Model and the Contribution of Gravity Waves. *Journal of Geophysical Research: Atmospheres*, **128**, e2022JD037907, https://doi.org/10.1029/2022JD037907.

Karpechko, A. Y., 2018: Predictability of sudden stratospheric warmings in the ECMWF extended-range forecast system. *Mon Weather Rev*, **146**, 1063–1075, https://doi.org/10.1175/MWR-D-17-0317.1.

Kay, J. E., and Coauthors, 2015: The community earth system model (CESM) large ensemble project : A community resource for studying climate change in the presence of internal climate variability. *Bull Am Meteorol Soc*, 1333–1349, https://doi.org/10.1175/BAMS-D-13-00255.1.

Kinoshita, T., Y. Tomikawa, and K. Sato, 2010: On the Three-Dimensional Residual Mean Circulation and Wave Activity Flux of the Primitive Equations. *Journal of the Meteorological Society of Japan*, **88**, 373–394, https://doi.org/10.2151/jmsj.2010-307.

Kodera, K., H. Mukougawa, P. Maury, M. Ueda, and C. Claud, 2016: Absorbing and reflecting sudden stratospheric warming events and their relationship with tropospheric circulation. *Journal of Geophysical Research: Atmospheres*, **121**, 80–94, https://doi.org/10.1038/175238c0.

Kuttippurath, J., and G. Nikulin, 2012: A comparative study of the major sudden stratospheric warmings in the Arctic winters 2003/2004-2009/2010. *Atmos Chem Phys*, **12**, 8115–8129, https://doi.org/10.5194/acp-12-8115-2012.

Lieberman, R. S., D. M. Riggin, and D. E. Siskind, 2013: Stationary waves in the wintertime mesosphere: Evidence for gravity wave filtering by stratospheric planetary waves. *Journal of Geophysical Research: Atmospheres*, **118**, 3139–3149, https://doi.org/10.1002/jgrd.50319.

Limpasuvan, V., J. H. Richter, Y. J. Orsolini, F. Stordal, and O. K. Kvissel, 2012: The roles of planetary and gravity waves during a major stratospheric sudden warming as characterized in WACCM. *J Atmos Sol Terr Phys*, **78–79**, 84–98, https://doi.org/10.1016/j.jastp.2011.03.004.

——, Y. J. Orsolini, A. Chandran, R. R. Garcia, and A. K. Smith, 2016: On the composite response of the MLT to major sudden stratospheric warming events with elevated stratopause. *J Geophys Res*, **121**, 4518–4537, https://doi.org/10.1002/2015JD024401.

Lindzen, R. S., B. Farrell, and K. K. Tung, 1980: The concept of wave overreflection and its application to baroclinic instability. *J Atmos Sci*, **37**, 44–63, https://doi.org/10.1175/1520-0469(1980)037<0044:TCOWOA>2.0.CO;2.

Manney, G. L., and Coauthors, 2008: The evolution of the stratopause during the 2006 major warming: Satellite data and assimilated meteorological analyses. *J Geophys Res*, **113**, D11115, https://doi.org/10.1029/2007jd009097.

——, and Coauthors, 2009: Aura Microwave Limb Sounder observations of dynamics and transport during the record-breaking 2009 Arctic stratospheric major warming. *Geophys Res Lett*, **36**, L12815, https://doi.org/10.1029/2009GL038586.

Marsh, D. R., M. J. Mills, D. E. Kinnison, J. F. Lamarque, N. Calvo, and L. M. Polvani, 2013: Climate change from 1850 to 2005 simulated in CESM1(WACCM). *J Clim*, **26**, 7372–7391, https://doi.org/10.1175/JCLI-D-12-00558.1.

Matsuno, T., 1971: A dynamical model of stratospheric sudden warming, *J Atmos Sci*, 1479–1494. https://doi.org/10.1175/1520-0469(1971)028<1479:ADMOTS>2.0.CO;2.

Orbe, C., Plummer, D., Waugh, D., Yang, H., Jöckel, P., Kinnison, D., Josse, B., Marecal, V., Deushi, M., Luke Abraham, N., Archibald, A., Chipperfield, M., Dhomse, S., Feng, W., & Bekki, S., 2020: Description and Evaluation of the specified-dynamics experiment in the Chemistry-Climate Model Initiative, *Atmospheric Chemistry and Physics*, ***20***, 3809–3840, https://doi.org/10.5194/acp-20-3809-2020.

O'Neill, A., and C. E. Youngblut, 1982: Stratospheric Warmings Diagnosed Using the Transformed Eulerian-Mean Equations and the Effect of the Mean State on Wave Propagation. *J Atmos Sci*, **39**, 1370–1386, https://doi.org/10.1175/1520-0469(1982)039<1370:swdutt>2.0.co;2.

Orsolini, Y. J., J. Urban, D.P. Murtagh, S. Lossow, and V. Limpasuvan, 2010: Descent from the polar mesosphere and anomalously high stratopause observed in 8 years of water vapor and temperature satellite observations by the Odin Sub-Millimeter Radiometer. *Journal of Geophysical Research: Atmospheres*, **115**, D12305. https://doi.org/10.1029/2009JD013501.

——, J. Zhang, V. Limpasuvan, 2022: Abrupt Change in the Lower Thermospheric Mean Meridional Circulation During Sudden Stratospheric Warmings and Its Impact on Trace Species. *Journal of Geophysical Research: Atmospheres*, **127**, e2022JD037050. https://doi.org/10.1029/2022JD037050.

——, V. Limpasuvan, K. Pérot, P. Espy, R. Hibbins, S. Lossow, K. Raaholt Larsson, and D. Murtagh, 2017: Modelling the descent of nitric oxide during the elevated stratopause event of January 2013. *J Atmos Sol Terr Phys*, **155**, 50–61, https://doi.org/10.1016/j.jastp.2017.01.006.

——, K. Nishii, and H. Nakamura, 2018: Duration and decay of Arctic stratospheric vortex events in the ECMWF seasonal forecast model. *Quarterly Journal of the Royal Meteorological Society*, 1–13, https://doi.org/10.1002/qj.3417.

Richter, J. H., F. Sassi, and R. R. Garcia, 2010: Towards a physically based gravity wave source parameterization in a general circulation model. *J. Atmos. Sci*., **67**, 136–156.

Rhodes, C. T., V. Limpasuvan, and Y. J. Orsolini, 2021: Eastward-Propagating Planetary Waves Prior to the January 2009 Sudden Stratospheric Warming. *J Geophys Res*, **126**, e2020JD033696. https://doi.org/10.1029/2020JD033696.

Sassi, F., H.-L. Liu, and J. T. Emmert, 2016: Traveling planetary-scale waves in the lower thermosphere: Effects on neutral density and composition during solar minimum conditions. *J Geophys Res Space Phys*, **121**, 1780–1801, https://doi.org/10.1002/2015JA022082.

Siskind, D. E., Eckermann, S. D., McCormack, J. P., Coy, L., Hoppel, K. W., & Baker, N. L., 2010: Case studies of the mesospheric response to recent minor, major, and extended stratospheric warmings. *Journal of Geophysical Research Atmospheres,* 115, D00N03. https://doi.org/10.1029/2010JD014114.

Smith, A. K., 2003: The Origin of Stationary Planetary Waves in the Upper Mesosphere. *Journal of Atmospheric Sciences*, **60**, 3033–3041, https://doi.org/10.1175/1520-0469(2003)060<3033:TOOSPW>2.0.CO;2.

Song, B. G., Chun, H. Y., & Song, I. S. (2020). Role of gravity waves in a vortex-split sudden stratospheric warming in January 2009. *Journal of the Atmospheric Sciences*, **77**, 3321–3342. https://doi.org/10.1175/JAS-D-20-0039.1.

Tomikawa, Y., K. Sato, S. Watanabe, Y. Kawatani, K. Miyazaki, and M. Takahashi, 2012: Growth of planetary waves and the formation of an elevated stratopause after a major stratospheric sudden warming in a T213L256 GCM. *Journal of Geophysical Research Atmospheres*, **117**, D16101, https://doi.org/10.1029/2011JD017243.